https://doi.org/10.1016/j.micromeso.2021.111092



# Evolution mechanisms and kinetics of porous structures during chemical dealloying of binary alloys

Jie Li[a], Shenyang Hu[b], Yulan Li[b], San-Qiang Shi[a,*]

[a]Department of Mechanical Engineering, The Hong Kong Polytechnic University, Hung Hom, Kowloon, Hong Kong, China

[b]Pacific Northwest National Laboratory, 902 Battelle Blvd., Richland, WA 99352, USA

## Abstract

Chemical dealloying beckons researchers both for scientific interest in corrosion failure of metallic materials and for the fabrication of nanoporous materials that have versatile applications due to their ultra-high surface area. Empirically, nanoporous structure evolves by the corrosion of less noble elements coupled with the rearrangement of more noble elements in the alloys. However, how topologically complex porous structures form and how environmental and material factors affect the dealloying kinetics are still unknown. This work develops a multi-phase-field model to demonstrate that a nucleation-growth mechanism can explain the formation of nanoporous structures under chemical attack. The evolution of nanoporous patterns from a binary alloy is examined as a function of the chemical content of the electrolyte, precursor alloy

* Corresponding author. Department of Mechanical Engineering, The Hong Kong Polytechnic University, Hung Hom, Kowloon, Hong Kong, China.

Email address: mmsqshi@polyu.edu.hk (San-Qiang Shi)

composition, dimensionality, and bulk and surface diffusion coefficients, which is validated with experimental observations. Two-phase composite dealloying and the effect of defect pre-existed in the precursor are also presented. The comprehensive model developed in this study provides a powerful tool to tailor made nanoporous metallic structures under chemical dealloying.

Keywords: Chemical dealloying; Multi-phase-field model; Nanoporous

## 1. Introduction

Dealloying refers to the process of removing one or more elements from multielement metals or metal composites, which has been studied as a potential tool for the fabrication of porous structures that have wide applications in catalytic activation, adsorption separation, energy storage, and sensing[1]–[5]. Corrosion-controlled techniques that involve controlled electrolytic corrosion and free corrosion—the so-called electrochemical and chemical dealloying, respectively—by immersing the alloy precursor and removing less noble (LN) elements from alloys in aqueous acid, alkaline, or salt solution with or without applied electropotential have been widely used to fabricate porous Au, Cu, Pt, and other metal structure networks[4]–[7]. Recently, liquid-metal and vapor-phase dealloying have been used to prepare porous structures through selective element melting or evaporation[8]–[10]. Essentially, all dealloying methods are based on the physical or chemical differences among different elements or components, such as their chemical potential, melting point, or vapor pressure to remove some elements from the alloys.

Thus, understanding the underlying pattern formation mechanisms during corrosion-controlled (chemical) dealloying is very important for better control and design of porous structures. Because it is difficult to observe the early stages of interfacial pattern formation and differentiate the effect of each factor experimentally, many theoretical and numerical approaches have been proposed to study the dealloying process. One early work assumed that both LN and MN elements dissolve simultaneously at the solid–liquid interface, LN elements are converted into ions flowing into the solution, and MN elements redeposit near the interface[11]. Pickering et al.[12] introduced a bulk diffusion mechanism, which assumed that the interface dissolution of LN elements creates vacancies, allowing the interior LN elements to move toward the surface layer

through vacancy diffusion. However, these two models made certain unreasonable assumptions and failed to exhibit consistency with the experimental results. Sieradzki et al.[13] found that the inherent percolation clusters comprising LN elements determine the porosity evolution. Erlebacher et al.[2] proposed that porosity evolution is a dynamical phase separation process and used the kinetic Monte Carlo (KMC) method to reproduce the porous evolution behavior of Ag-Au alloy. However, they did not consider the effects of some controlling parameters. Moreover, the largest size of the dealloying system and timeframe that KMC can handle is limited[14]. Other theoretical modeling studies on porous metals include ab initio method and molecular dynamics study for investigating the physical and mechanical properties of porous metals [15], [16]. Thus, a comprehensive theoretical framework that can capture the fundamental mechanisms controlling the kinetics of dealloying and quantitatively predict the morphology of porous evolution during chemical dealloying is urgently required.

Over the last two decades, phase-field model (PFM) has rapidly advanced as a mesoscale modeling method, and has been used to predict many physical processes, such as dendrite evolution, solute segregation, electrochemical deposition, crack propagation, and void evolution in materials[17]. Using the fundamental thermodynamic and kinetic information as the input, PFM can predict the evolution of arbitrary morphologies and complex microstructures without explicitly tracking the positions of the interfaces. A few studies have attempted to reproduce the corrosion process and investigate the factors influencing the process using PFM. Mai et al.[18] used a PFM to simulate the pitting corrosion based on the Kim–Kim–Suzuki model by calibrating the interface kinetics parameter with the exchange current density. On the same basis, Ansari et al.[19] incorporated the effects of the overpotential, cathodic

reaction, chemical reaction, and physical processes occurring in the electrolyte. Recently, this group of researchers further developed multi-phase-field models to study pitting corrosion with an insoluble corrosion product[20] and intergranular corrosion of sensitized metals[21]. However, all these studies assumed the dissolution of the entire metal, and did not consider the cases where the noble elements in the metals stay in the solid phase during corrosion. Benefiting from the research progress of PFM for solidification, Geslin et al.[8] developed a PFM to capture the formation of porous Ta during a liquid-metal dealloying process of Ta–Ti in the liquid Cu melt. They used an Allen–Cahn equation to capture the solid–liquid surface evolution and Cahn–Hilliard equations to describe the metal transport in the liquid phase. However, so far, little progress has been made on the mesoscale modeling of metal porosity kinetics during a general corrosion-controlled dealloying using a PFM.

In this study, we develop a thermodynamically consistent theoretical and computational multi-PFM to investigate the chemical dealloying behavior of Au–Ag alloy. The remainder of this paper is organized as follows. In the methods section, the formulation of a multi-PFM for the alloy-Au clusters-electrolyte system is detailed. The system's Gibbs free energy comprises the chemical and interfacial free energy. The generalized Allen–Cahn equations and modified Cahn–Hilliard equations are constructed to govern the topological interface and metal concentration evolutions. In the results section, the fundamental dealloying behavior and evolution mechanism are analyzed based on 1D, 2D, and 3D simulation cases. Next, simulations are conducted for a set of samples with different dealloying conditions to shed light on the morphological differences dependent on the corrosion agent, initial alloy composition, dimensionality, surface diffusion coefficients, inert phase and pre-existing defects in the precursor and also compared with the experimental results.

## 2. Method

### 2.1. Investigated system

The model system studied here consists of $\mathrm{Ag}_{1-c_0}\mathrm{Au}_{c_0}$ binary alloy immersed in nitric acid solutions shown in Fig. 1. The etching of alloy starts from the free corrosion of Ag via the following reaction[22]:

$$\mathrm{Ag} + 2\mathrm{HNO_3} \rightarrow \mathrm{AgNO_3} + \mathrm{NO_2} + \mathrm{H_2O}, \tag{1}$$

The corrosion rate is governed by the Arrhenius Law:

$$R_1 = k_0 c_{\mathrm{Ag}} \exp\left(\frac{-G}{RT}\right) \tag{2}$$

Here, $k_0$ is the reaction constant, $c_{\mathrm{Ag}}$ is the molar fraction of silver, $R$ is the gas constant, $T$ is the absolute temperature, and $G$ is the reaction activation energy dependent on the acid concentration in the electrolyte phase and initial composition of the alloy. Then undissolved Au atoms do not reside in original sites but aggregate into nanoscale clusters in the solid-liquid interface. In addition to bulk diffusion and two interface processes described above, an overall chemical dealloying process also involves long-range mass-transport processes (inflow of corrosive electrolyte into the porous structure and outflow of dissolved ions through the electrolyte). Many experimental studies, based on a constant current response measured when an electrical potential is applied, have testified that the dealloying velocity is approximately constant, indicating that long-range mass-transport processes are very fast, and thus, do not control the porous structure evolution during the chemical dealloying of Ag-Au[23]–[25]. Therefore, in this study, we assume that the formation and evolution of a porous structure are dominated by the two interface processes, and that the long-range mass-transport processes can be ignored.

To test the agreement between the experimental observations and simulation results, we choose a set of alloys with different initial Au compositions ($c_0$ = 0.2, 0.25, 0.3, and 0.35) for the numerical tests. The nitric acid solutions are set with four different concentrations ($c_a$ = 9.1, 10.9, 12.7, and 14.6 mol/L). We assign the value obtained from reference[26] to the reaction activation barrier ($G$) in the dealloying process of $Ag_{0.7}Au_{0.3}$ alloy immersed in nitric acid solution with a concentration of $c_a$ = 10.9 mol/L and calibrate the reaction constant $k_0$ by approximating the simulated dealloying velocity to the experimental value[23]

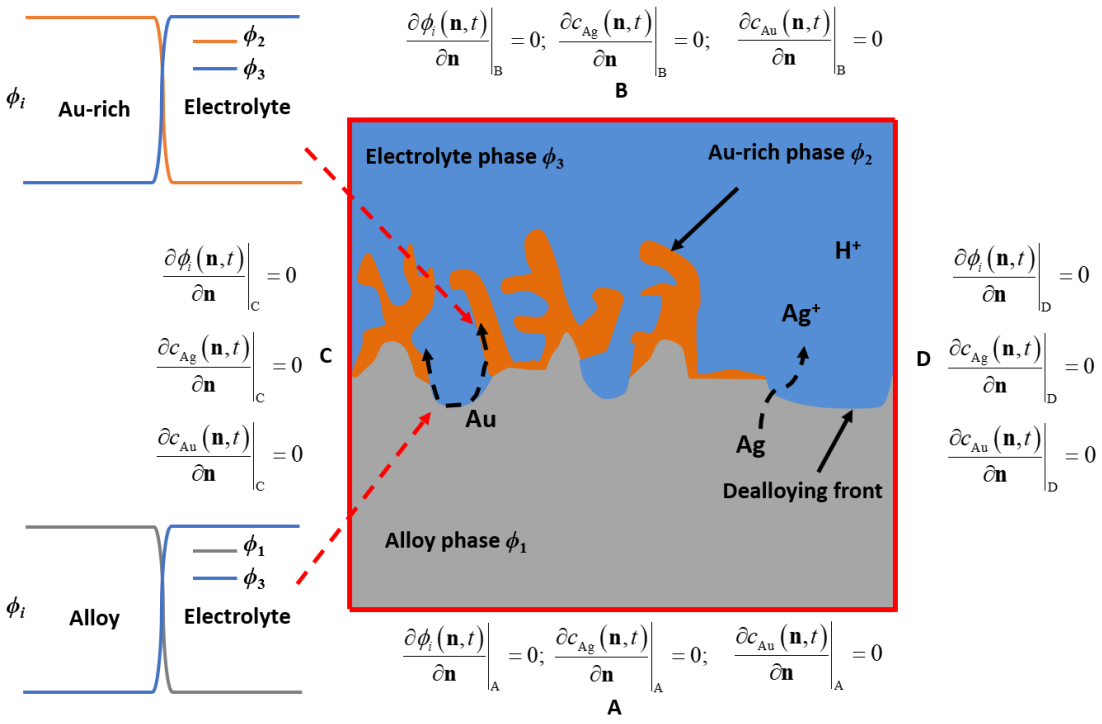


Fig. 1. Schematics of the chemical dealloying process of Ag–Au alloy and boundary conditions

The results obtained from the extensive body of experiments show that the solid–liquid interface comprises passivated porous clusters linked by pits, where the alloy is attacked by the electrolyte. In the Au–Ag system, the aggregation of Au clusters is essential for the topological interface morphology. Erlebacher et al. presented an interfacial spinodal

decomposition mechanism to explain the coalescence of Au clusters[2]. In this mechanism, Ag is dissolved from the solid-liquid interface due to the corrosion process, while the undissolved Au atoms are released into the interface layer. The Au atoms and electrolyte in this interface layer are considered as two conserved variables in a regular solution. As the concentration of Au in this interface layer is much above its solubility in the electrolyte, Au clusters are formed within the spinodal decomposition region. There is, however, another possible mechanism, Au cluster nucleation and growth, where the interface layer lies in the metastable region. The aggregation of nearly pure Au clusters is a thermally activated process, which means that the nucleation of Au clusters in the interface layer requires overcoming an energy barrier.

### 2.2. Multi-phase-field model

Based on this Au nucleation and growth mechanism, we use three order parameters $\phi_i$ ($i$ = 1, 2, 3) and two concentration parameters ($c_{\mathrm{Ag}}$ and $c_{\mathrm{Au}}$) to describe the microstructures in the system with three coexisting phases at the interface: Ag–Au alloy phase ($\phi_1$, $c_{\mathrm{Ag}}$, $c_{\mathrm{Au}}$), Au-rich phase ($\phi_2$, $c_{\mathrm{Ag}}$, $c_{\mathrm{Au}}$), and electrolyte phase ($\phi_3$, $c_{\mathrm{Ag}}$, $c_{\mathrm{Au}}$). Note that $c_{\mathrm{Ag}} \approx 0$ in the Au-rich phase and $c_{\mathrm{Au}} \approx 0$ in the electrolyte phase. $\phi_i$ is used to spatially differentiate the three coexisting phases and satisfy the normalization condition of $\sum_{i=1}^{3} \phi_i = 1$. Within the individual phases, $\phi_i$ has a constant value of 1 inside phase $i$ and 0 outside phase $i$, and smoothly varies from 1 to 0 across the phase interface.

PFM describes the microstructure evolution of heterogeneous materials toward the reduction in the thermodynamic energy functional of the system, which comprises free energy of the bulk phases and interfaces. Here, to avoid an unexpected formation of the third phase (the electrolyte) in a pairwise interface, following reference[27], the total free-energy functional of the system is expressed as

$$F = \int \left( \frac{\varepsilon}{2} \sum_i \left( \nabla \phi_i \right)^2 + W \sum_i \phi_i^2 \left( 1 - \phi_i \right)^2 + f_{\text{chem}} \left( \phi_i, c_{\text{Ag}}, c_{\text{Au}} \right) \right) dV , \quad (3)$$

where the first term corresponds to the gradient energy density at the interfaces, the second term indicates the potential barrier between the bulk phases, and the last term describes their chemical free-energy density. Furthermore, the gradient energy coefficient, $\varepsilon$, and potential well height, $W$, are defined as $\varepsilon = \frac{\sigma l}{4\sqrt{2}a}$ and $W = \frac{a\sqrt{2}}{4} \sigma / l$, where $a$ is a numerical constant, $l$ is the interface thickness, and $\sigma$ is the interface energy[18]. We assume the same interface property for different interfaces in the system. Although we aim to match the experimental observations as much as possible, we also aim to develop a model for the general behavior of interface topology evolution of porous structures using the minimum number of parameters to elucidate the essential processes during the dealloying.

As shown in Eq. (4), the chemical free energy is developed using a mixture rule, which assumes that the interfacial region is occupied by a mixture of three phases, with the fraction of $h_i$ for the $i$ phase. The interpolation function $h_i$ can be formulated as $h_i = \phi_i^2 \Big/ \sum_j \phi_j^2$ to fulfill the thermodynamic consistency requirement, which meets $\sum_j h_j = 1$ and $dh_j / d\phi_i = 0 (\phi_i = 0,1)$. We define the free-energy density of phase $i$, $f_{\text{chem}}^i$, as a parabolic form in terms of $c_{\text{Ag}}^i$ and $c_{\text{Au}}^i$, which are the compositions of Ag and Au in $\phi_i$ using Eq. (5). $c_{\text{Ag}}^i$ and $c_{\text{Au}}^i$ are not independent of each other, but constrained by the conditions of Eqs. (6) and (7). These conditions enforce that the interfacial region be composed of coexisting phases with different compositions but equal chemical potential for all components. $c_{\text{Ag,e}}^i$ and $c_{\text{Au,e}}^i$ are the normalized

equilibrium concentrations of Ag and Au elements for the three phases shown in Table 1, and $c_0$ is the initial alloy composition of the alloy phase (alloy precursor). Note that the initial alloy can be considered to be in a quasi-equilibrium state, although the values of the equilibrium concentrations in the alloy phase used in the simulations are different from the concentrations corresponding to the minimum values of free energy. *A* and *B* in Eq. (5) are the thermodynamic factors, which are assumed to be equal for the three phases, for simplicity. Because the parabolic form of chemical free-energy density in Eq. (5) is an approximation of the real chemical free-energy functional, we suggest to select the thermodynamic factors based on the nucleation energy of the porous Au-rich phase.

$$f_{\text{chem}} = \sum_{i=1}^{3} h_i f_{\text{chem}}^{i}(c_{\text{Ag}}^{i}, c_{\text{Au}}^{i}) \tag{4}$$

$$f_{\text{chem}}^{i} = A\left(c_{\text{Ag}}^{i} - c_{\text{Ag,e}}^{i}\right)^2 + B\left(c_{\text{Au}}^{i} - c_{\text{Au,e}}^{i}\right)^2 \tag{5}$$

$$c_{\text{Ag}} = \sum_{i=1}^{3} h_i c_{\text{Ag}}^{i}, \frac{\partial f_{\text{chem}}^{1}}{\partial c_{\text{Ag}}^{1}} = \frac{\partial f_{\text{chem}}^{2}}{\partial c_{\text{Ag}}^{2}} = \frac{\partial f_{\text{chem}}^{3}}{\partial c_{\text{Ag}}^{3}} = \mu_{\text{Ag}} \tag{6}$$

$$c_{\text{Au}} = \sum_{i=1}^{3} h_i c_{\text{Au}}^{i}, \frac{\partial f_{\text{chem}}^{1}}{\partial c_{\text{Au}}^{1}} = \frac{\partial f_{\text{chem}}^{2}}{\partial c_{\text{Au}}^{2}} = \frac{\partial f_{\text{chem}}^{3}}{\partial c_{\text{Au}}^{3}} = \mu_{\text{Au}} \tag{7}$$

$$\frac{\partial \phi_i}{\partial t} = -\frac{1}{3}\sum_{j \neq i} L\left(\frac{\delta F}{\delta \phi_i} - \frac{\delta F}{\delta \phi_j}\right) + \xi_{\phi_2} \tag{8}$$

$$\frac{\delta F}{\delta \phi_i} = -\frac{\varepsilon}{2}\nabla^2 \phi_i + W\phi_i\left(1-\phi_i\right)\left(1-2\phi_i\right) + \Omega_i \tag{9}$$

$$\Omega_i = \sum_j \frac{\partial h_j}{\partial \phi_i}\left(f_{\text{chem}}^{j}\left(c_{\text{Ag}}^{j}, c_{\text{Au}}^{j}\right) - \mu_{\text{Ag}} c_{\text{Ag}}^{j} - \mu_{\text{Au}} c_{\text{Au}}^{j}\right) \tag{10}$$

$$\xi_{\phi_2} = \xi_0 r 16\phi_1^2\left(1-\phi_1\right)^2 I_0 k_B T\, \Delta\Omega_{23}^2 / \sigma^3 \tag{11}$$

Table 1 Equilibrium compositions of Ag and Au in three phases

| Phases / Components | Alloy phase ($\phi_1$) | Au phase ($\phi_2$) | Electrolyte phase ($\phi_3$) |
|---|---|---|---|
| Ag | 1-$c_0$ | 0 | 0 |
| Au | $c_0$ | 1 | 0 |

Then, the kinetic equations for the spatial and temporal evolutions of $\phi_i$ can be expressed as Eqs. (8) and (9), where $L$ indicates the phase-field kinetic mobility and $\Omega_i$ indicates the grand potential of phase $\phi_i$. In Eq. (8), the nucleation of the Au phase at the solid–liquid interface is attributable to the thermal fluctuations in the interfacial layer, which is incorporated into the model through a noise term, $\xi_{\phi_2}$, expressed as Eq. (11). In this equation, $r \in (-1,1)$ is a random number assigned to the alloy interface in each time and space step, and $\xi_0$ is the strength of the fluctuations. The heterogeneous nucleation is explicitly incorporated into the system by assuming a nucleation rate that follows $I = I_0 \exp\left(-G^* / \left(k_B T\right)\right) \approx I_0\, k_B T / G^*$. According to the classical nucleation theory, $I_0$ is the nucleation prefactor, $k_B$ is the Boltzmann constant, and $G^*$ is the critical nucleation energy, expressed as $G^* = \sigma^3 / \Delta\Omega_{23}^2$. Thus, this term introduces the fluctuations in $\phi_2$ at the $\phi_1/\phi_3$ interface with an amplitude that is proportional to the chemical driving force $\Delta\Omega_{23} = \Omega_2 - \Omega_3$ and inversely proportional to the interface energy.

Then, for conserved concentration fields, the governing equations using the modified Cahn–Hilliard equation can be expressed as follows:

$$\frac{\partial c_{\mathrm{Ag}}}{\partial t} = \nabla M_{\mathrm{Ag}} \nabla \frac{\delta F}{\delta c_{\mathrm{Ag}}} + \lambda_1 R_1 = \nabla D_{\mathrm{Ag}} \sum_i h_i \nabla c_{\mathrm{Ag}}^i + \lambda_1 R_1 \tag{12}$$

$$\frac{\partial c_{\mathrm{Au}}}{\partial t} = \nabla M_{\mathrm{Au}} \nabla \frac{\delta F}{\delta c_{\mathrm{Au}}} = \nabla D_{\mathrm{Au}} \sum_i h_i \nabla c_{\mathrm{Au}}^i \tag{13}$$

$$D_{\mathrm{Ag}} = \sum_{i=1}^{3} h_i D_{\mathrm{Ag}}^i + \lambda_1 D_{\mathrm{Ag}}^{\mathrm{s}}, \quad D_{\mathrm{Au}} = \sum_{i=1}^{3} h_i D_{\mathrm{Au}}^i + \lambda_2 D_{\mathrm{Au}}^{\mathrm{s}} \tag{14}$$

The first terms of Eqs. (12) and (13) describe the diffusion of Ag and Au in the solid. As expressed in Eq. (14), the diffusion of all metal atoms involves the bulk diffusion in *i* phase with respective diffusivities of $D_{\mathrm{Ag}}^i$ and $D_{\mathrm{Au}}^i$ and interface diffusion with diffusivities of $D_{\mathrm{Ag}}^{\mathrm{s}}$ and $D_{\mathrm{Au}}^{\mathrm{s}}$. The last term of Eq. (12) represents the corrosion rate of Ag at the metal–electrolyte interface. .$\lambda_1$ and $\lambda_2$ in Eqs. (12) and (14) are expressed as $\lambda_1 = 4h_1h_3$ and $\lambda_2 = 4(h_1h_3 + h_2h_3)$, indicating that the interface behavior of the LN elements is appreciable only in the vicinity of the alloy–electrolyte interface and that the surface diffusion of MN elements occurs at pairwise interfaces (including alloy–electrolyte and Au–electrolyte interfaces). The diffusion path of MN element or the binary interfaces involved in this process is described in Fig. 1. The values of all parameters used in the simulations are listed in Table 2.

In two dimensions, the system has a size of 90 × 100 nm$^2$, and the liquid domain is set with an initial depth of 10 nm. The boundary conditions are given in Fig. 1. The boundary conditions in 1D and 3D cases are the same as those in 2D cases. The zero-flux boundary conditions are applied on all sides or surfaces of the system. Uniform square-mesh elements are chosen to discretize the space with $\Delta x = l/10$ and $\Delta x = l/4$ for 1D and 2D systems ($l$ is the interface thickness), respectively. The size of alloy domain in 3D geometry is 40 × 30 ×20 nm$^3$. Tetrahedral mesh elements are used to discretize 3D systems by using COMSOL Multiphysics. The Galerkin method is used as the finite element discretization method[28]. The backward differentiation formula

is used for the time integration of the governing equations[29].

Table 2 Parameters used in the simulations

| | Parameter | Value |
|---|---|---|
| Interfacial energy density | $\sigma$ (J/ m$^2$) | 1 |
| Interface thickness | $l$ (nm) | 2 |
| Kinetic interface parameter | $L$ (m$^3$/J/s) | $1.5 \times 10^{-6}$ |
| Bulk diffusion coefficient of Ag in the alloy phase | $D_{Ag}^{1}$ (m$^2$/s) | $10^{-20}$ |
| Bulk diffusion coefficient of Au in the alloy phase | $D_{Au}^{1}$ (m$^2$/s) | $10^{-20}$ |
| Bulk diffusion coefficient of Ag in the Au-rich phase | $D_{Ag}^{2}$ (m$^2$/s) | $10^{-20}$ |
| Bulk diffusion coefficient of Au in the Au-rich phase | $D_{Au}^{2}$ (m$^2$/s) | $10^{-20}$ |
| Surface diffusion coefficient of Ag | $D_{Ag}^{s}$ (m$^2$/s) | $10^{-16}$~ $10^{-13}$ |
| Surface diffusion coefficient of Au | $D_{Au}^{s}$ (m$^2$/s) | $10^{-16}$~ $10^{-13}$ |
| Free-energy density curvature | $A$ (J/m$^3$) | $3 \times 10^9$ |
| Free-energy density curvature | $B$ (J/m$^3$) | $15 \times 10^9$ |
| Ideal gas constant | $R$ (J/mol/K) | 8.314 |
| Absolute temperature | $T$ (K) | 300 |

| | | |
|---|---|---|
| Numerical constant | $a$ | 2.94 |
| Nucleation prefactor | $I_0$ | $10^5$ |
| Reaction constant | $k_0$ | $1.87 \times 10^{19}$ |

## 3. Results

### 3.1. 1D simulation

A 1D model is first implemented to simulate the evolution of the planar dealloying frontier shown in Fig. 2; in this case, a binary alloy $Ag_{0.7}Au_{0.3}$ immersed in 10.9 mol/L nitric acid is used. After dealloying for 10 s, the dealloying frontier is observed to be occupied by a mixture of three phases. At the dealloying frontier, most of the Ag element is dissolved, while the Au element, as shown in Fig. 2(a), is confined to the surface layer, leading to a buildup of Au and the formation of $\phi_2$. The gradual accumulation of the Au element, driven by surface diffusion, blocks the corrosion of Ag, leading to a decrease in the Ag dissolution flux and a noticeable retardation of the dealloying front propagation, as shown in Fig. 2(b). Therefore, in a 1D system, the corrosion of Ag is reduced by Au accumulation at the solid-liquid interface. In addition, extracting the peak concentration of the Au element ($c_{Au}^{p}$) from the interface layer, we find that the dealloying velocity ($v$) decreases exponentially with $c_{Au}^{p}$, which is consistent with the 1D simulation results of the liquid-metal dealloying in reference[8], where the unmelted element accumulated at the solid–liquid interface.

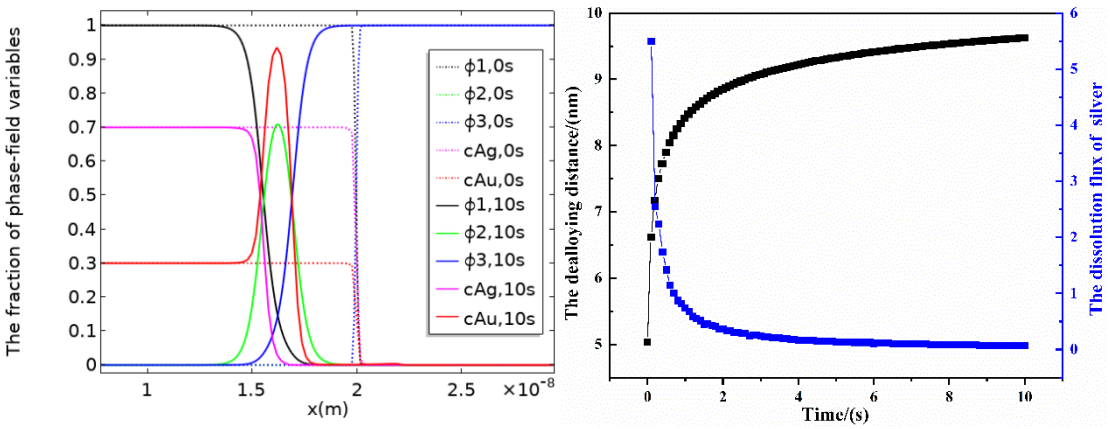


(a) (b)

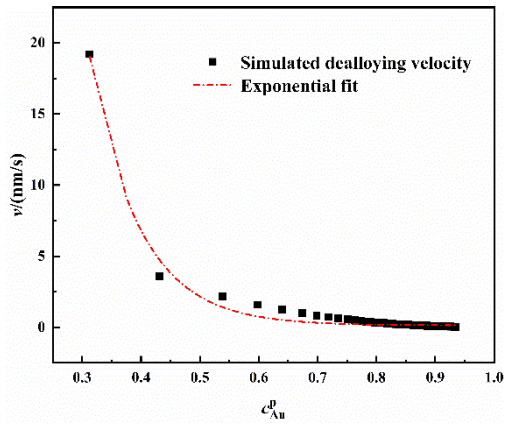


(c)

Fig. 2. One-dimensional simulation result for $Ag_{0.7}Au_{0.3}$ immersed in 10.9 mol/L nitric acid at $t$ = 10 s: (a) evolution of phase-field variables, (b) dealloying front position and dissolution flux of Ag as functions of time, and (c) dealloying velocity as a function of the peak concentration of Au in the solid–liquid interface layer.

### 3.2. 2D simulation of the nucleation and growth of Au-rich clusters at the interface during dealloying

Unlike the 1D case where the Au accumulation hinders the dealloying frontier advancement, the Au buildup can cause the lateral formation of Au-rich phases along the alloy–electrolyte interface in 2D. Fig. 3 shows the periodic distribution of the Au-rich phase at an early stage of dealloying with different noise amplitudes, where $\phi_1$ is

presented in blue, $\phi_2$ in yellow, and $\phi_3$ in red. The figure shows that the nucleation of $\phi_2$ perturbs the stability of the planar dealloying front. Moreover, it shows that a stronger magnitude of $\xi_0$ can shorten the nucleation incubation period and increase the nucleation density, while not affecting the thermodynamic characteristics substantially[30]. It is challenging to observe the initial density of the ligaments experimentally, making it difficult to calibrate the amplitude of the noise term according to the experimental results. Here, to improve the computation stability, we choose a smaller amplitude in the following simulations.

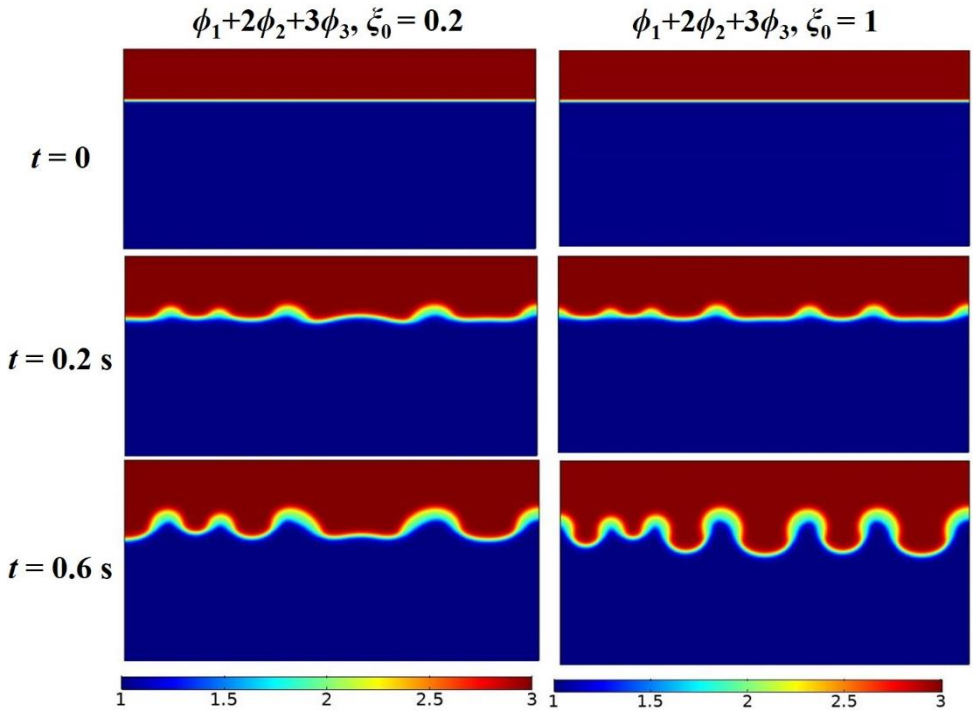


Fig. 3. Two-dimensional simulation results for the nucleation events in $Ag_{0.7}Au_{0.3}$ dealloyed in nitric acid solution with a concentration of $c_a$ = 10.9 mol/L, showing the formation of Au-rich clusters and initial growth at the solid–liquid interface (left column: $\xi_0$ = 0.2; right column: $\xi_0$ = 1).

To clarify the subsequent evolution of the phases and structure during the dealloying process, snapshots of the microstructures for alloy $Ag_{0.7}Au_{0.3}$ at different times, as well

as the metal concentrations, are shown in Fig. 4. The nucleation stage leaves etched pits between the Au-rich clusters. These pits become vulnerable sites where the Ag atoms are exposed to the electrolyte and more Ag atoms are corroded out of the alloy, releasing more Au atoms into the interface layer. Owing to the fast surface diffusion of Au atoms, the Au clusters grow in size, and sometimes, smaller clusters are absorbed by the larger clusters. Such coarsening is fundamentally driven by the reduction in free energy, which is naturally incorporated in PFM. With the continual invasion of the acid solution, some of these Au ligaments finally detach from the alloy, as their basements have a composition equal to that of the virgin alloy. Moreover, certain self-assembled core/shell ligaments with a pure Au surface and alloy interior can be observed. At this point, we can define a characteristic spacing distance $\lambda$ separating these ligaments, which is on the order of 10 nm in length. Note that unlike the connected porous structure observed through in-plane scanning electron microscopy[31], [32], here, the simulated 2D structure corresponds to the cross-sectional view of the dealloyed sample.

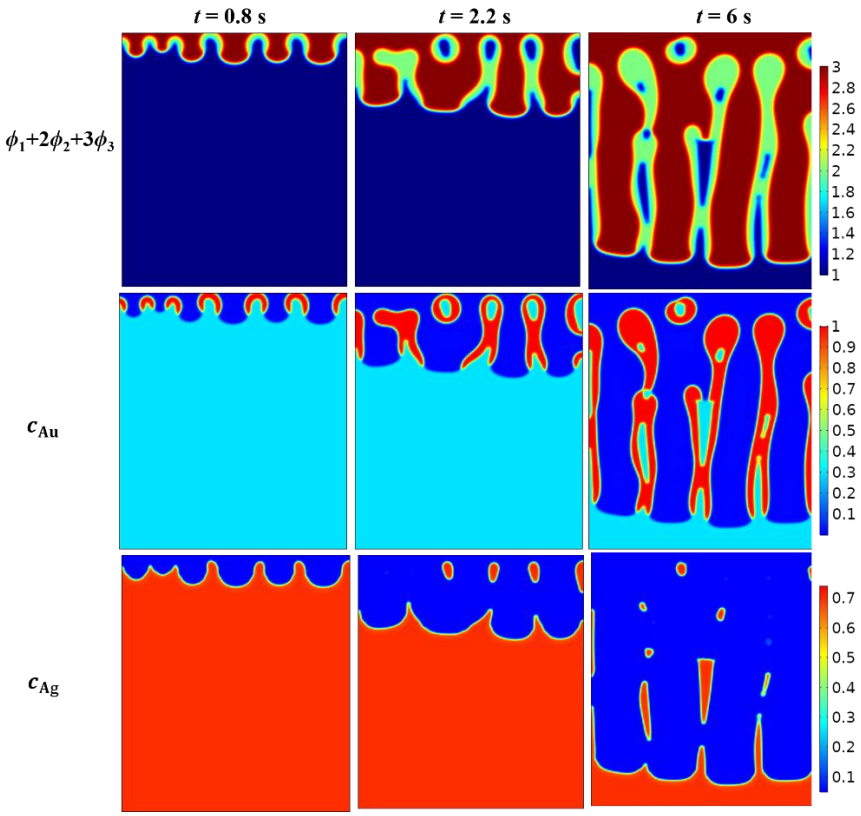


Fig. 4. Snapshots of 2D porous morphology evolution for $Ag_{0.7}Au_{0.3}$ immersed in nitric acid solution with a concentration of $c_a$ = 10.9 mol/L.

### 3.3. Effect of chemical content of the electrolyte and precursor alloy composition

Two interface-relevant processes(corrosion and interface diffusion) are found to be decisive for the length scale of porosity, which implies that any dealloying condition that affects the interface behaviors can be treated as a controllable parameter for tailoring the porous structure with desirable morphology and composition. In this section, we focus on the parameters that affect the dissolution rate of LN elements. Experimentally, a marked boundary separating the porous structure from the virgin alloy, known as the dealloying front, is observed. By tracking the dealloying front as a function of time, we can quantitatively evaluate the dealloying kinetics. We assume that the effect of the nitric acid concentration on the reaction activation energy follows the below linear relation:

$$G = G_0 + k_1 c_a \,, \tag{15}$$

where the characteristic parameters can be calibrated as $G_0 = 1.154$ eV and $k_1 = -0.0099$ for $Ag_{0.7}Au_{0.3}$ dealloyed at $c_a$ = 9.1 and 10.9 mol/L by approximating the simulated dealloying rate to the experimental value[23]. Using these calibrated values, we perform simulations with different acid concentrations ($c_a$ = 9.1, 10.9, 12.7, and 14.6 mol/L). In each case, three simulations with the same noise amplitude but different random seed numbers are conducted. Fig. 5(a) plots a graph of the dealloying depth vs. the dealloying time by tracking the position of the contour line of $\phi_1 = 0.5$ at the ligament roots near the dealloying front. The dealloying fronts in all cases travel the same maximum distance. The relation between the dealloying front position and time can be approximated by linear functions, where the slopes provide the dealloying front propagation rate. Fig. 5(b) indicates that the dealloying front velocity increases exponentially with the concentration of nitric acid, which agrees well with the experimental data.

We also establish a similar function as Eq. (15) to incorporate the effect of the precursor alloy composition, because a linear correlation between the precursor alloy composition and reaction activation energy is found in the experiments reported in reference[26]. For the numerical tests, we choose a set of alloys with different initial Au compositions ($c_0$ = 0.2, 0.25, 0.3, and 0.35). In each alloy, three simulations with the same noise amplitude but different random seeds are also conducted. A series of constant dealloying-front evolution processes dependent on the initial alloy composition is observed in Fig. 6(a). These results are in good agreement with those obtained for the in situ imaging measurements, which implies that the present PFM correctly reproduces the dealloying kinetics. Note that due to the lack of experimental measurement, the combined effect of alloy composition and acid concentration is difficult to calibrate,

and thus, beyond the scope of this paper.

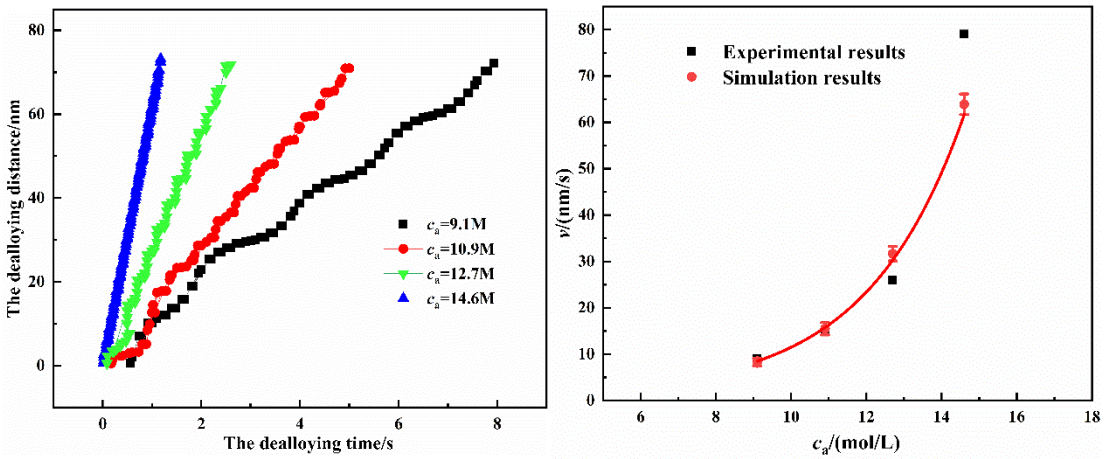


(a) (b)

Fig. 5. Two-dimensional simulation results for the evolution of dealloying front in $Ag_{0.7}Au_{0.3}$ immersed in electrolytes with different acid concentrations: (a) predicted dealloying distance vs. time ; (b) comparison with experimental results[23].

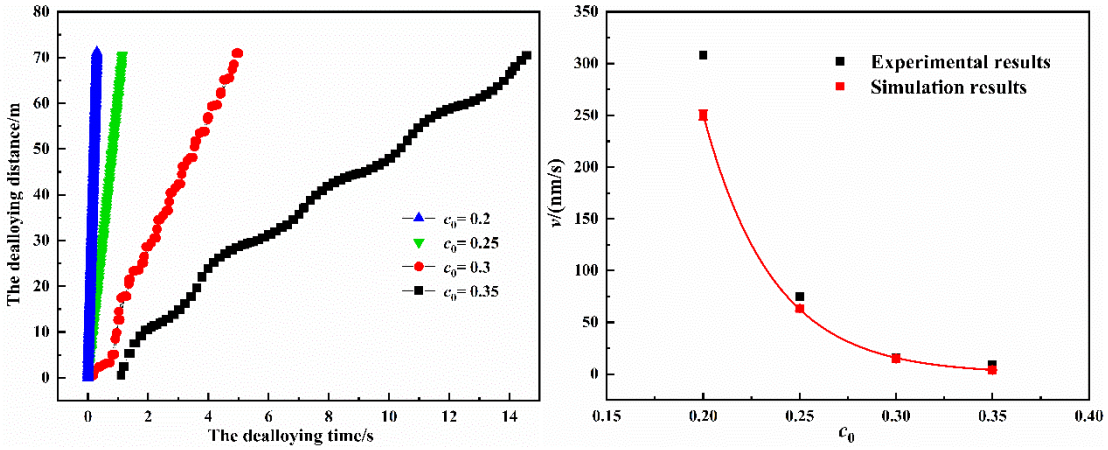


(a) (b)

Fig. 6. Two-dimensional simulation results for the evolution of dealloying front in $Ag_{1-c_0}Au_{c_0}$ immersed in the electrolyte with $c_a$ = 10.9 mol/L: (a) predicted dealloying distance vs. time; (b) comparison with experimental results[23].

The simulated microstructure morphologies of $Ag_{0.7}Au_{0.3}$ in different acid solutions

when the dealloying fronts travel to the same depths are shown in Fig. 7. The ligaments with thickness ranging from 3 to 25 nm penetrate the entire dealloyed area. When the alloy is exposed to an electrolyte with a high acid concentration, the dealloying front advances too quickly to enable the MN elements to passivate the alloy, resulting in a higher density of pure Au ligaments with smaller thickness, and is more likely to detach from the dense alloy. In contrast, in a low-concentration acid, the Ag dissolution rate is low, and thus, Au atoms have more opportunity to passivate the original alloy, resulting in much thicker ligaments with core/shell structures. In the following, these alloy trapped inside the core of ligaments will be further exposed into the electrolyte by a diffusive restructuring of these formed ligaments, while the dealloying front continually proceeds into the master alloy. Many experiments have shown that the fraction of residual Ag in the dealloyed structure decreases concurrently with the coarsening of ligaments during chemical dealloying, which indicates that structure coarsening contributes to the further etching of alloy[33], [34]. The etching of dealloyed ligaments is similar to the dealloying of nanoparticles. However, the latter operates by a vacancy diffusion mechanism by which Ag diffuses into the surface layer via a Kirkendall effect, causing a hollow core-shell structure, which has not happened[35], [36]. The simulation here also found that the change of bulk diffusion coefficient has no effect on the nanoporosity evolution. This verifies that the coarsening of ligaments mainly arises from the surface diffusion of Au atoms, leading to the collapse of some ligaments onto adjacent ones and further dissolution of the alloy during this secondary dealloying step. Besides the ligament size, the ligament spacing also scales with the acid concentration, as illustrated in Fig. 7; the higher is the acid concentration, the smaller is the ligament spacing.

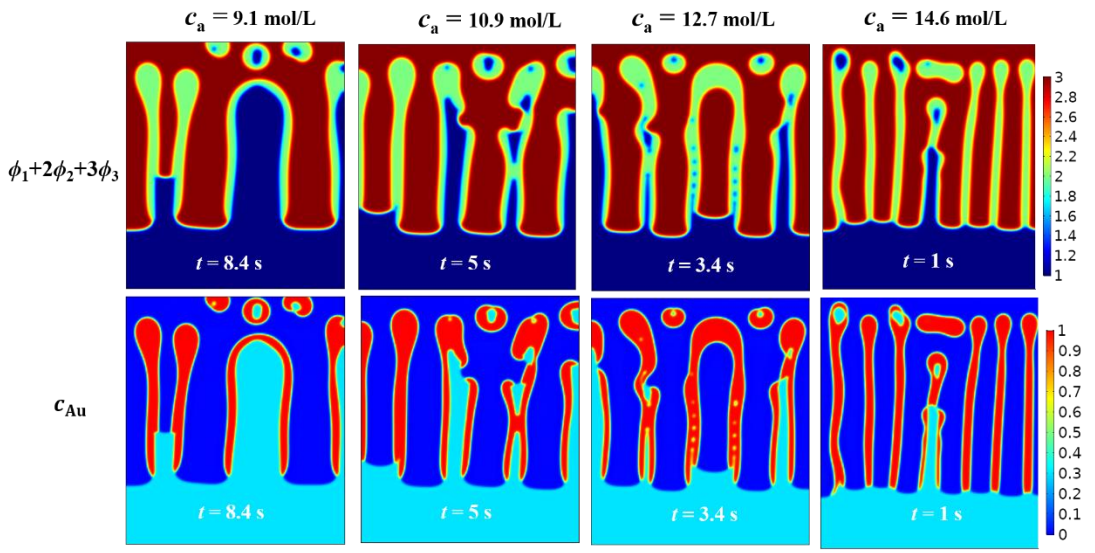


Fig. 7. Effect of acid concentration on microstructure evolution for $Ag_{0.7}Au_{0.3}$ in 2D geometry.

Fig. 8 presents the simulated microstructure when the dealloying fronts travel the same depths of different initial alloys in the same acid solution. It can be seen that the lower is the Au content, the smaller are the ligament thickness and ligament spacing. The content threshold (or parting limit) of the initial alloy originally defines the ratio of MN elements, above which the electrochemical dealloying is hindered by a passive layer of MN elements irrespective of applied potential[37]. The content threshold for fcc binary alloy is usually found to be 40 ~ 50 at% according to the percolation model, KMC simulation, and experimental observations[23], [38]. In situ imaging [23] found that $Ag_{0.6}Au_{0.4}$ achieved a shallow dealloying depth before the dealloying front stopped. An experiment in Ref [39] reported that the chemical dealloying of Ag-Au is weakened when $c_0$ is greater than 0.4, manifested in a slight increase of Au content after dealloying. However, there has been no microscopic evidence of passivation, making it difficult to determine the content threshold. Fig. 8 shows that $Ag_{0.55}Au_{0.45}$ presents a surface shallow dealloying. This is because the dissolution of Ag is slow, and more Au atoms spread on the surface, preventing the development of porosity evolution. In contrast,

for the leanest alloy ($c_0$ = 0.2), the ligaments fall apart into small nanoscaled blobs due to the fast corrosion rate and insufficient Au content in the initial alloy. Hence, this model provides a convenient tool to determine the parting limits (or content thresholds) for porous formation during chemical dealloying.

To study the morphology differences dependent on the dimensionality in detail, 3D microstructures of the precursors with different initial composition are shown in Fig. 9. The first column shows the structure evolution of three phases ($\phi_1$, grey; $\phi_2$, red; $\phi_3$, blue) in a transparent mode in each case. The hidden of the liquid phase in the second column can better present the dealloyed structure. In order to observe the alloy remained in the ligaments, the iso-value surface of $\phi_1$ = 0.5 and iso-concentration surface of $c_{Au}$ = 0.5 are shown in the third column of Fig. 9. Similar to the 2D results described above, the dealloying velocity increases with the decrease of $c_0$. The size of the ligaments increases with $c_0$, and more alloy relics are wrapped in the ligaments when the dealloying fronts pass over the distance. However, the 3D ligaments appear as nanoscale entanglements with a random network arrangement and present better connectivity than in 2D geometries because there is more topological genus associated with interface instabilities and bifurcation in a 3D geometry. Animations of the cases in Fig. 9, $S_1$, $S_2$, $S_3$, and $S_4$, are also available in Supplementary Material to better visualize the dealloying process.

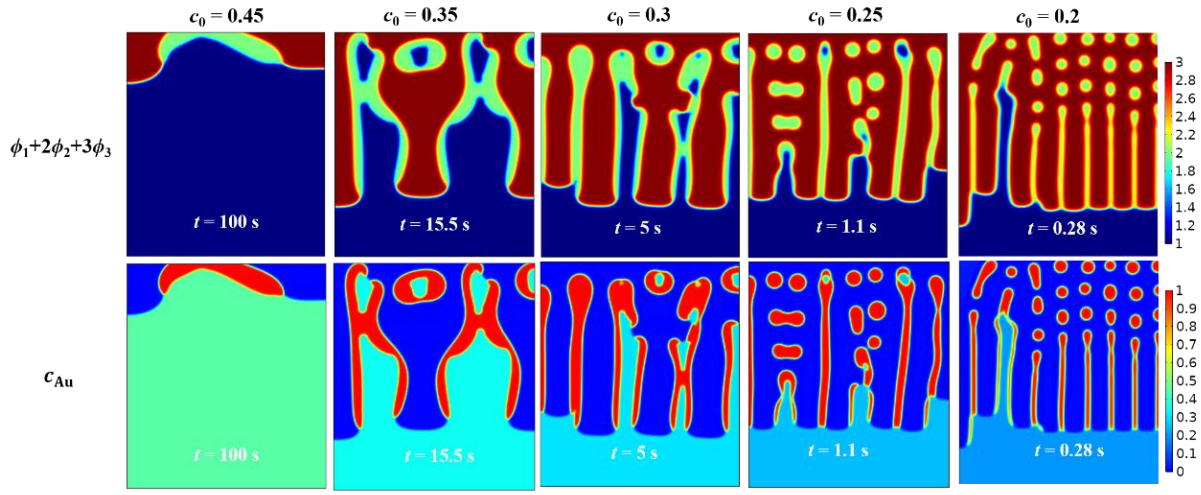


Fig. 8. Microstructure evolution for a set of alloys with different initial compositions dealloyed in an electrolyte of $c_a$ = 10.9 mol/L in 2D geometry.

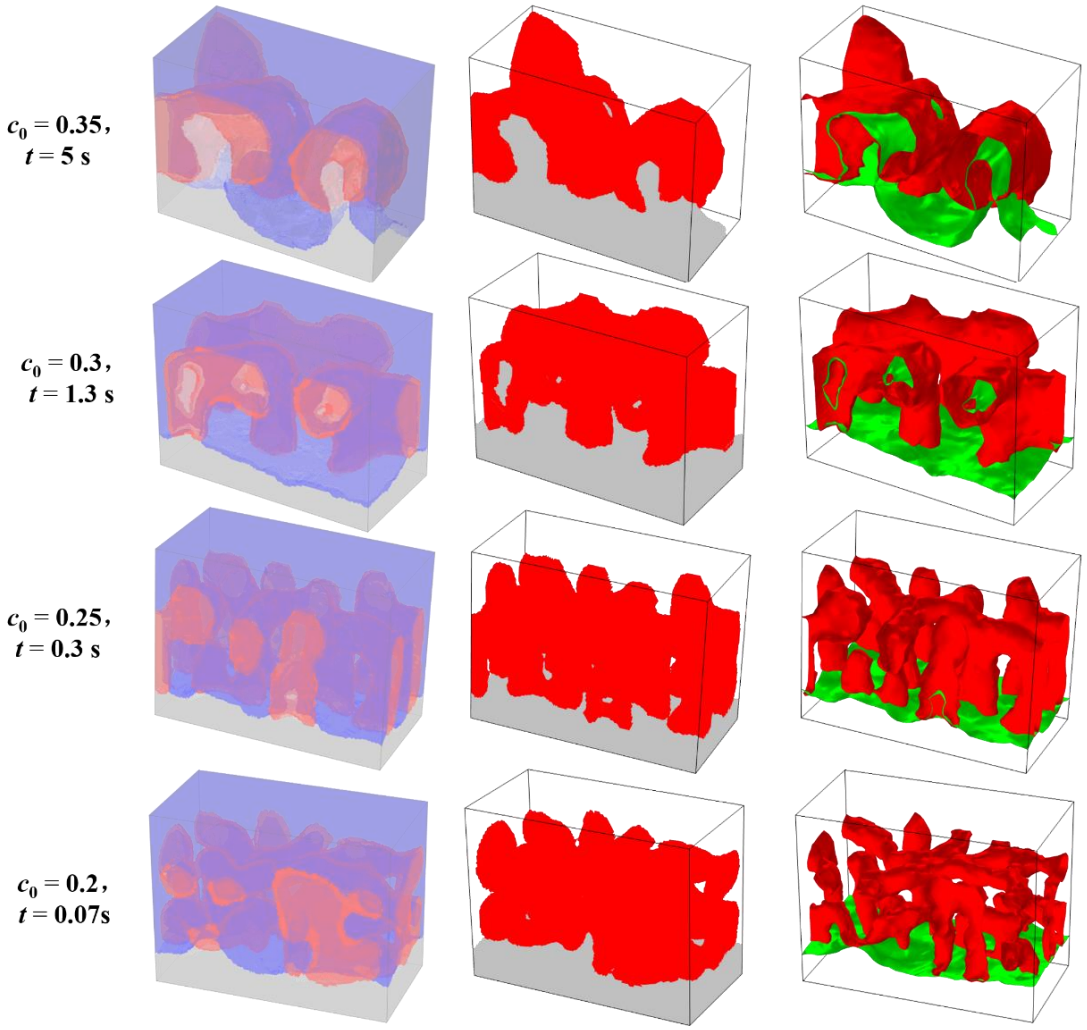

Fig. 9. 3D microstructure evolution for $Ag_{1-c_0}Au_{c_0}$ dealloyed in the electrolyte of $c_a$ = 10.9 mol/L: the first column shows all phases during porous formation (alloy phase: gray; Au-rich phase: red; electrolyte phase: blue); the second column shows the evolution of the Au-rich phase (red) and electrolyte phase (blue); in the third column, the green surface represents an iso-value surface of $\phi_1 = 0.5$, demarcating the dealloying front, and the red surface represents an iso-concentration surface of $c_{Au} = 0.5$, demarcating the Au-rich phase.

Owing to the limitation of the simulated areas, it is difficult to extract reliable quantitative and statistically meaningful information on the characteristic length scale of the porous structure from the above 2D simulations. However, the apparent distinction in morphology, associated with a set of samples dealloyed under different conditions, yields a qualitative comparison analysis by extracting the characteristic size of ligament spacing. Fig. 10 confirms a decrease in the ligament spacing with an increase in the acid concentration and Ag content. The average ligament spacing in each case can be calculated by sampling the distances between the centerline of the ligaments in all simulations with different random seeds. As there is no related quantitative research on the evolution of ligament spacing in 2D cross-section morphology, we try to ensure consistency in the magnitude with the previous experiments[31], [32]. Note that due to the limited connectivity in 2D geometry and simulation time, the ligament coarsening of the ligaments cannot be adequately observed; thereby, the potential variation in ligament spacing along the dealloying depth is ignored. The data presented in Fig. 10 indicate the ligament spacing at the dealloying front. Such predictions are consistent with the experimental observations as well as the KMC simulations, which show that the ligament spacing decreases with increasing electropotential[2], [14], [31].

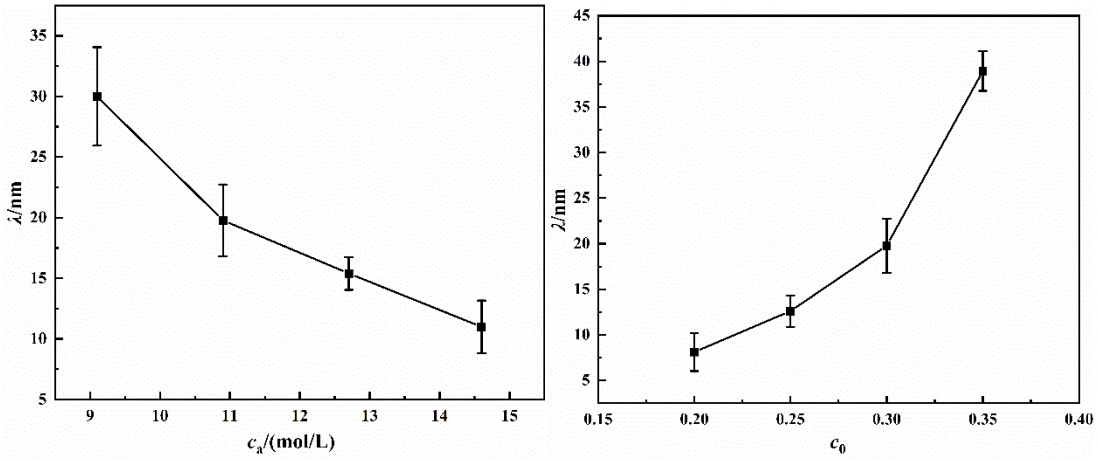


(a) (b)

Fig. 10. Effects of acid and alloy concentrations on ligament spacing in 2D geometry.

### 3.4. Effect of surface diffusion coefficient

Many studies have shown that the addition of halides to the electrolyte can increase the ligament spacing, and estimated that the surface diffusivity of Au is three orders of magnitude higher with the addition of KI halide than that without it[40]. In addition, it has been found that a low dealloying temperature results in an ultrafine nanoporous structure[41]. Hence, we investigate the role of diffusion of MN elements in the dealloying process by varying the value of the surface diffusion coefficient. The resultant structures are shown in Fig. 11. Many previous studies have focused on the measurement of the surface diffusion coefficient of Au element in electrolyte solutions, but have obtained considerably different results[13], [37], [40], [42]. The measurement results are substantially dependent on the electrochemical surface reaction system, absorbates of the electrolyte solutions, and surface geometry. Moreover, compared with the coarsening stage, Au atoms can aggregate into clusters more quickly when they are just released by Ag corrosion. Here, we assign the same value to the surface diffusivity of Ag and Au as that obtained from reference[13], after making a curvature correction. As shown in Fig. 10, when the diffusion coefficient is $2 \times 10^{-15}$ $m^2/s$, the surface

diffusion of the MN elements is too slow, and thus, the Au atoms can neither form clusters nor provide liquid paths for Ag corrosion to proceed, thus leaving a Au passivation layer on the alloy surface. This result is similar to that obtained by Hakamada et al.[43], who reported that during the electrical dealloying of $Pd_{0.2}Co_{0.8}$, the Pd aggregation appeared to be inhibited, resulting in passivity, even after the application of sufficient electrode potential. Upon increasing the value of the surface diffusion coefficient, the aggregation of MN elements forms Au clusters and the corrosion process continues through the creation of a contact area with the electrolyte. Therefore, the rapid surface diffusion of MN elements is essential for the formation and evolution of a porous structure. Furthermore, the dealloyed structure exhibits an inverse relation with the surface diffusion coefficient: the higher is the surface diffusion coefficient, the thicker are the ligaments and the larger is their spacing.

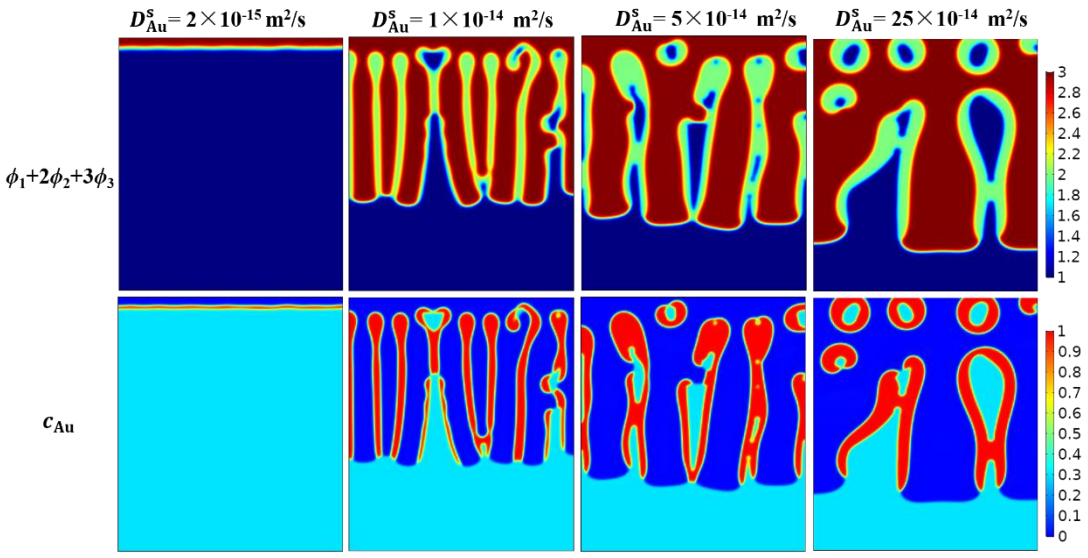


Fig. 11. Effect of surface diffusivity of Au and Ag on microstructure morphology in $Ag_{0.7}Au_{0.3}$ dealloyed in the electrolyte of $c_a$ = 10.9 mol/L at $t$ = 5 s.

Although the size, spacing, and composition of the ligaments vary with the dealloying conditions, in each case of a different characteristic length, the morphology presents a

eutectic structure evolution process. The changes in the dealloyed structure with respect to the precursor alloy and acid concentration can be quantitatively assessed by the interface diffusion behavior of MN elements. Based on the theoretical study in reference[8], the characteristic ligament spacing of the nanoporous structure in liquid-metal dealloying is predicted as $\lambda \propto \sqrt{D_{\mathrm{Au}}^{\mathrm{s}}/(vc_0)}$, which is also observed in our simulations. Although liquid-metal dealloying is controlled by the diffusion of the miscible element in liquid, the ligament spacing is controlled by diffusion and the mass conservation law both in the liquid-metal dealloying and chemical dealloying, as shown in Fig. 12. As an example of $Ag_{0.7}Au_{0.3}$ dealloyed at $c_a$ = 9.1, 10.9, 12.7, and 14.6 mol/L, Fig. 12(a) indicates that $\lambda$ is proportional to $1/\sqrt{v}$. Fig. 12(b) validates the scaling law through the linear fit between $\lambda$ and $1/\sqrt{(vc_0)}$ for $Ag_{1-c_0}Au_{c_0}$ ($c_0$ = 0.2, 0.25, 0.3, 0.35) dealloyed at $c_a$ = 10.9 mol/L. Fig. 12(c) provides a linear fit between $\lambda$ and $\sqrt{D_{\mathrm{Au}}^{\mathrm{s}}/v}$ in the case of $Ag_{0.7}Au_{0.3}$ dealloyed at $c_a$ = 10.9 mol/L with different surface diffusivities for Au ($D_{\mathrm{Au}}^{\mathrm{s}}$ = 1 × $10^{-14}$ $m^2/s$, 5 × $10^{-14}$ $m^2/s$, 25 × $10^{-14}$ $m^2/s$).

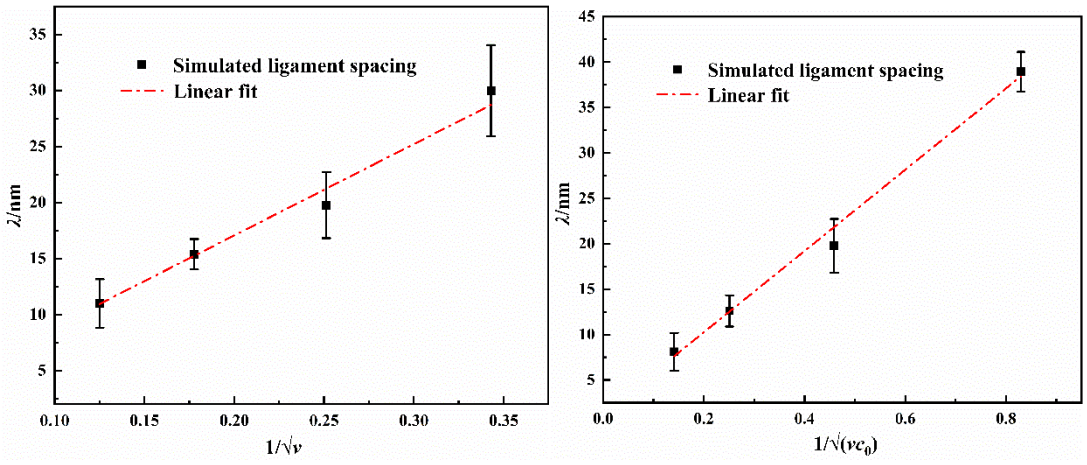


(a) (b)

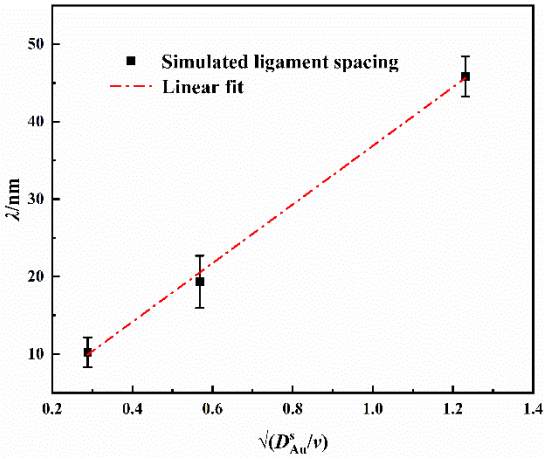


(c)

Fig. 12. Validation of ligament spacing law. (a) Effect of acid concentration on ligament spacing for $Ag_{0.7}Au_{0.3}$, $\lambda \propto 1/\sqrt{v}$; (b) effect of alloy composition on ligament spacing, $\lambda \propto 1/\sqrt{vc_0}$, for $Ag_{1-c_0}Au_{c_0}$ in acid of concentration 10.9 mol/L; and (c) the effect of surface diffusion coefficient on ligament spacing, $\lambda \propto \sqrt{D_{Au}^s/v}$, for $Ag_{0.7}Au_{0.3}$ in acid of concentration 10.9 mol/L; the red dashed lines indicate linear fits.

### 3.5. Dealloying of two-phase composite and effect of defect pre-existed in precursor

The experimental findings showed that the variety of precursors determines the diversity of dealloying-made nanoporous structures. Liu et al.[7] reviewed the formation of nanoporous copper with different ligament-channel structures from dual-phase alloy families comprising solid solution and intermetallics and the potential of nanoporous copper with suitable pore size distributions when working as electrodes. Wang et al.[44] also fabricated nanoporous Pd composites through the chemical dealloying of Al-Pd alloy composed of two phases ($Al_3Pd$ and $Al_3Pd_2$). The resultant nanoporous Pd composites consist of nanoporous Pd matrix dealloyed from $Al_3Pd$ phase and undealloyed $Al_3Pd_2$ embeddings and possess high electrocatalytic activities. Here, we model the chemical dealloying process of binary alloy with the presence of a

second phase. We add a second phase with random shapes into the $Ag_{0.7}Au_{0.3}$ matrix for simplicity. We consider two cases where the second phase is inert or active. To ensure that the inert phase is stable during dealloying, we apply the Dirichlet boundary condition ($\phi_1 = 1$) to the inert phase. When the second phase is active, we assume it is composed of pure LN elements, and the dealloying of two-composites can be used to produce a bimodal porous structure. The relevant parameters can be calibrated with experiments for different binary alloys. Fig. 13(a) shows that dealloyed structure comprises a porous matrix and compact embeddings, while Fig. 13(b) presents a large size channel structure coupled with porous walls, which demonstrates the capability of this model to reproduce the dealloying morphology of two-phase precursors. Since our model is a multi-phase model, the model can be easily extended to study composites that have more than two phases.

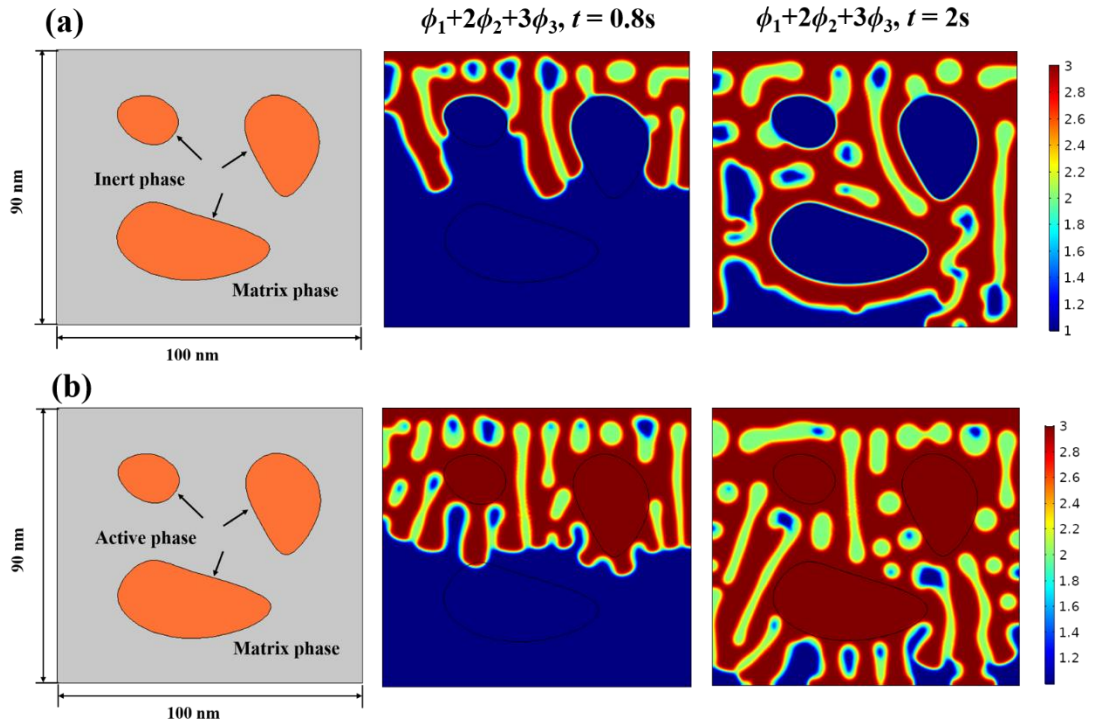


Fig. 13. Microstructure evolution for the chemical dealloying of two-phase composites

Experiments also showed that pre-existing defects in the precursors, such as voids,

grain boundaries, and segregations, will affect the rate of dealloying. The active element located at those defective sites with disordered atom arrangement may corrode faster than that at the matrix[23]. To ensure the electrochemical difference between matrix and defective sites, we assign a higher activation energy that is four times the reaction activation energy of matrix to defective sites. Fig. 14 shows that the dealloying front is no longer planar, and the etching near defective sites is faster than that in matrix. Moreover, the size of ligaments close to defective sites is smaller due to the increase of dealloying velocity, which has been illustrated in the previous section.

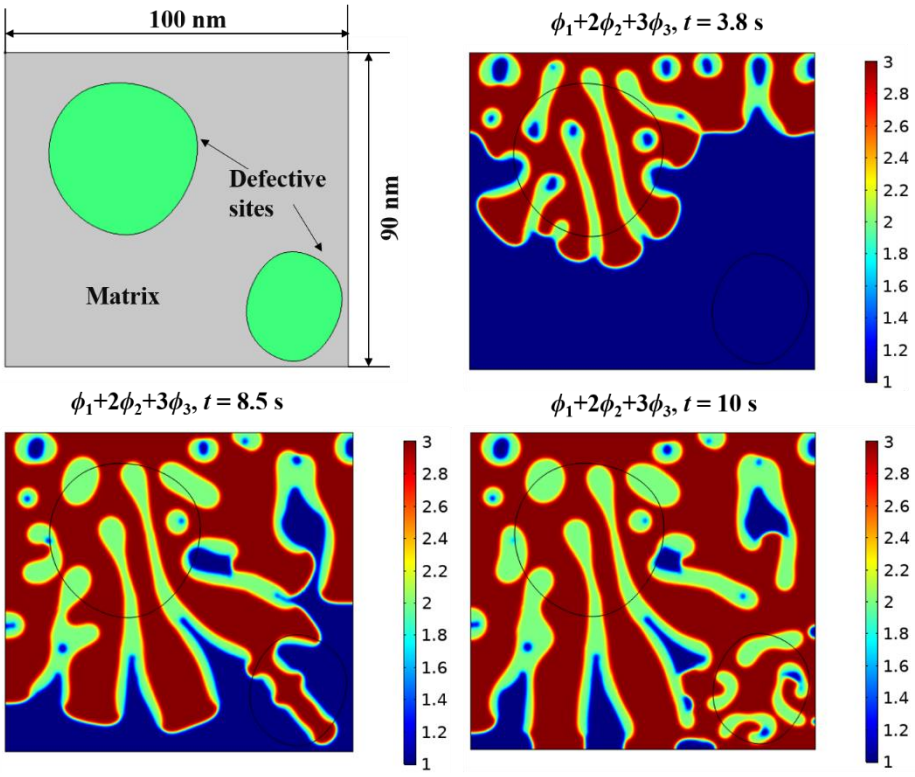


Fig. 14. Effect of defective sites pre-existed in the precursor on the microstructure evolution during chemical dealloying process

## 4. Conclusions

The chemical dealloying can generate topologically complex and diverse nanoporous structures with great application potential. In this study, a multiphase-field model based

on a nucleation-growth mechanism is developed to understand and predict this behavior of Au–Ag alloy. The nucleation of the porous phase is controlled by a noise term, which is scaled by the phase transformation driving force to account for the heterogeneous nucleation. At the growth stage of the porous structure, the model focuses on two major interface-related processes: corrosion of the LN element (Ag) and surface diffusion of the MN element (Au). The simulation results demonstrate that the interplay between the Ag dissolution and Au diffusion determines the dealloying kinetics and morphology of the porous structure. The parameters affecting the interface processes, such as the chemical acid concentration, initial alloy composition, and surface diffusion coefficient, are demonstrated to be the key factors controlling the morphology evolution of the dealloyed structure, which mirrors the experimentally observed behaviors. We also demonstrate the capability of this model to determine the content thresholds (parting limits) for porous structure formation, and to simulate the dealloying of two-phase composite and precursor with the presence of defects. This study improves our fundamental understanding of porous structure development and provides meaningful guidance and tools for the design and development of new porous metals by chemical dealloying for achieving special applications in different fields.

## Acknowledgments

This study was supported by a grant from the Research Grants Council of Hong Kong (PolyU 152174/17E).

## References

[1] M. Stratmann and M. Rohwerder, “A pore view of corrosion,” *Nature*, vol. 410, no. 6827, pp. 420–423, 2001, doi: 10.1038/35068652.

[2] J. Erlebacher, M. J. Aziz, A. Karma, N. Dimitrov, and K. Sieradzki, “Evolution of nanoporosity in dealloying,” *Nature*, vol. 410, no. 6827, pp. 450–453, 2001, doi: 10.1038/35068529.

[3] Q. Chen, Y. Ding, and M. Chen, “Nanoporous metal by dealloying for electrochemical energy conversion and storage,” *MRS Bull.*, vol. 43, no. 1, pp. 43–48, 2018, doi: 10.1557/mrs.2017.300.

[4] Y. Ding, Y. J. Kim, and J. Erlebacher, “Nanoporous gold leaf: ‘ancient technology’/advanced material,” *Adv. Mater.*, vol. 16, no. 21, pp. 1897–1900, 2004, doi: 10.1002/adma.200400792.

[5] I. McCue, E. Benn, B. Gaskey, and J. Erlebacher, “Dealloying and dealloyed Materials,” *Annu. Rev. Mater. Res.*, vol. 46, no. 1, pp. 263–286, 2016, doi: 10.1146/annurev-matsci-070115-031739.

[6] H. Galinski *et al.*, “Dealloying of platinum-aluminum thin Films: Dynamics of pattern formation,” *Phys. Rev. Lett.*, vol. 107, no. 22, pp. 6–9, 2011, doi: 10.1103/PhysRevLett.107.225503.

[7] W. Liu, L. Chen, J. Yan, N. Li, S. Shi, and S. Zhang, “Nanoporous copper from dual-phase alloy families and its technology application in lithium ion batteries,” *Corros. Rev.*, vol. 33, no. 5, pp. 203–231, 2015, doi: 10.1515/corrrev-2014-0066.

[8] P. A. Geslin, I. McCue, B. Gaskey, J. Erlebacher, and A. Karma, “Topology-generating interfacial pattern formation during liquid metal dealloying,” *Nat. Commun.*, vol. 6, pp. 1–8, 2015, doi: 10.1038/ncomms9887.

[9] I. McCue, B. Gaskey, P. A. Geslin, A. Karma, and J. Erlebacher, “Kinetics and morphological evolution of liquid metal dealloying,” *Acta Mater.*, vol. 115, pp. 10–23, 2016, doi: 10.1016/j.actamat.2016.05.032.

[10] Z. Lu *et al.*, “Three-dimensional bicontinuous nanoporous materials by vapor phase dealloying,” *Nat. Commun.*, vol. 9, no. 1, pp. 1–7, 2018, doi: 10.1038/s41467-017-02167-y.

[11] H. Kaesche, *Metallic corrosion: principles of physical chemistry and current problems*. Houston, Tex.: National Association of Corrosion Engineers, 1985.

[12] H. W. Pickering, “Volume diffusion during anodic dissolution of a binary alloy,” *J. Electrochem. Soc.*, vol. 115, no. 2, pp. 143–147, 1968, doi: 10.1149/1.2411048.

[13] K. Sieradzki, “Curvature Effects in Alloy Dissolution,” *J. Electrochem. Soc.*, vol. 140, no. 10, pp. 2868–2872, 1993, doi: 10.1149/1.2220924.

[14] J. Erlebacher, “An atomistic description of dealloying porosity evolution, the critical potential, and rate-limiting behavior,” *J. Electrochem. Soc.*, vol. 151, no. 10, pp. 614–626, 2004, doi: 10.1149/1.1784820.

[15] T. Fujita *et al.*, “Atomic origins of the high catalytic activity of nanoporous gold,” *Nat. Mater.*, vol. 11, no. 9, pp. 775–780, 2012, doi: 10.1038/nmat3391.

[16] J. F. Rodriguez-Nieva and E. M. Bringa, “Molecular dynamics and Monte Carlo simulations of the sputtering of a nanoporous solid,” *Nucl. Instruments Methods Phys. Res. Sect. B Beam Interact. with Mater. Atoms*, vol. 304, pp. 23–26, 2013, doi: 10.1016/j.nimb.2013.04.005.

[17] L. Q. Chen, “Phase-field models for microstructure evolution,” *Annu. Rev. Mater. Sci.*, vol. 32, pp. 113–140, 2002, doi: 10.1146/annurev.matsci.32.112001.132041.

[18] W. Mai, S. Soghrati, and R. G. Buchheit, “A phase field model for simulating the pitting corrosion,” *Corros. Sci.*, vol. 110, pp. 157–166, 2016, doi: 10.1016/j.corsci.2016.04.001.

[19] T. Q. Ansari, Z. Xiao, S. Hu, Y. Li, J. L. Luo, and S. Q. Shi, “Phase-field model of pitting corrosion kinetics in metallic materials,” *NPJ Comput. Mater.*, vol. 4, no. 1, pp. 1–9, 2018, doi: 10.1038/s41524-018-0089-4.

[20] T. Q. Ansari, J.-L. Luo, and S.-Q. Shi, “Modeling the effect of insoluble corrosion products on pitting corrosion kinetics of metals,” *NPJ Mater. Degrad.*, vol. 3, no. 1, pp. 1–12, 2019, doi: 10.1038/s41529-019-0090-5.

[21] T. Q. Ansari, J.-L. Luo, and S.-Q. Shi, “Multi-Phase-Field Model of Intergranular Corrosion Kinetics in Sensitized Metallic Materials,” *J. Electrochem. Soc.*, vol. 167, no. 6, p. 061508, 2020, doi: 10.1149/1945-7111/ab856d.

[22] C. Özmetin, M. Çopur, A. Yartasi, and M. M. Kocakerim, “Kinetic investigation of reaction between metallic silver and nitric acid solutions,” *Chem. Eng. Technol.*, vol. 23, no. 8, pp. 707–711, 2000, doi: 10.1002/1521-4125(200008)23:8<707::AID-CEAT707>3.0.CO;2-L.

[23] Y. C. K. Chen-Wiegart, S. Wang, I. McNulty, and D. C. Dunand, “Effect of Ag-Au composition and acid concentration on dealloying front velocity and cracking during nanoporous gold formation,” *Acta Mater.*, vol. 61, no. 15, pp. 5561–5570, 2013, doi: 10.1016/j.actamat.2013.05.039.

[24] N. A. Senior and R. C. Newman, “Synthesis of tough nanoporous metals by controlled electrolytic dealloying,” *Nanotechnology*, vol. 17, no. 9, pp. 2311–2316, 2006, doi: 10.1088/0957-4484/17/9/040.

[25] Y. C. K. Chen-Wiegart, S. Wang, W. K. Lee, I. McNulty, P. W. Voorhees, and D. C. Dunand, “In situ imaging of dealloying during nanoporous gold formation by transmission X-ray microscopy,” *Acta Mater.*, vol. 61, no. 4, pp. 1118–1125, 2013, doi: 10.1016/j.actamat.2012.10.017.

[26] J. Snyder and J. Erlebacher, “Kinetics of Crystal Etching Limited by Terrace Dissolution,” *J. Electrochem. Soc.*, vol. 157, no. 3, p. C125, 2010, doi: 10.1149/1.3280299.

[27] J. Kundin, E. Pogorelov, and H. Emmerich, “Phase-field modeling of the microstructure evolution and heterogeneous nucleation in solidifying ternary Al–Cu–Ni alloys,” *Acta Mater.*, vol. 83, pp. 448–459, 2015, doi: 10.1016/j.actamat.2014.09.057.

[28] G. Fairweather, *Finite element Galerkin methods for differential equations*. New York, NY : Dekker: Dekker, 1978.

[29] U. M. Ascher and L. R. Petzold, “Computer Methods for Ordinary Differential Equations and Differential-Algebraic Equations,” 1997.

[30] T. W. Heo and L. Q. Chen, “Phase-field modeling of nucleation in solid-state phase transformations,” *JOM*, vol. 66, no. 8, pp. 1520–1528, 2014, doi: 10.1007/s11837-014-1033-9.

[31] E. Detsi, M. Van De Schootbrugge, S. Punzhin, P. R. Onck, and J. T. M. De Hosson, "On tuning the morphology of nanoporous gold," *Scr. Mater.*, vol. 64, no. 4, pp. 319–322, 2011, doi: 10.1016/j.scriptamat.2010.10.023.

[32] M. C. Dixon, T. A. Daniel, M. Hieda, D. M. Smilgies, M. H. W. Chan, and D. L. Allara, "Preparation, structure, and optical properties of nanoporous gold thin films," *Langmuir*, vol. 23, no. 5, pp. 2414–2422, 2007, doi: 10.1021/la062313z.

[33] T. Krekeler *et al.*, "Silver-rich clusters in nanoporous gold," *Mater. Res. Lett.*, vol. 5, no. 5, pp. 314–321, 2017, doi: 10.1080/21663831.2016.1276485.

[34] X. L. Ye, N. Lu, X. J. Li, K. Du, J. Tan, and H. J. Jin, "Primary and secondary dealloying of Au(Pt)-Ag: Structural and compositional evolutions, and volume shrinkage," *J. Electrochem. Soc.*, vol. 161, no. 12, pp. C517–C526, 2014, doi: 10.1149/2.0131412jes.

[35] J. X. Wang *et al.*, "Kirkendall Effect and Lattice Contraction in Nanocatalysts: A New Strategy to Enhance Sustainable Activity," *J. Am. Chem. Soc*, vol. 133, pp. 13551–13557, 2011, doi: 10.1021/ja204518x.

[36] L. Dubau *et al.*, "Further insights into the durability of Pt3Co/C electrocatalysts: Formation of 'hollow' Pt nanoparticles induced by the Kirkendall effect," *Electrochim. Acta*, vol. 56, no. 28, pp. 10658–10667, 2011, doi: 10.1016/j.electacta.2011.03.073.

[37] R. C. Newman, S. G. Corcoran, J. Erlebacher, M. J. Aziz, and K. Sieradzki, "Alloy corrosion," *MRS Bull.*, vol. 24, no. 7, pp. 24–28, 1999, doi: 10.1557/S0883769400052660.

[38] D. M. Artymowicz, J. Erlebacher, and R. C. Newman, "Philosophical Magazine Relationship between the parting limit for de-alloying and a particular geometric high-density site percolation threshold Relationship between the parting limit for de-alloying and a particular geometric high-density site percolatio," *Philos. Mag.*, vol. 89, no. 21, pp. 1663–1693, 2009, doi: 10.1080/14786430903025708.

[39] X. Lu, E. Bischoff, R. Spolenak, and T. J. Balk, "Investigation of dealloying in Au-Ag thin films by quantitative electron probe microanalysis," *Scr. Mater.*, vol. 56, no. 7, pp. 557–560, 2007, doi: 10.1016/j.scriptamat.2006.12.022.

[40] A. Dursun, D. V. Pugh, and S. G. Corcoran, "Dealloying of Ag-Au alloys in halide-containing electrolytes. Affect on critical potential and pore size," *J. Electrochem. Soc.*, vol. 150, no. 7, pp. 0–5, 2003, doi: 10.1149/1.1580824.

[41] L. H. Qian and M. W. Chen, "Ultrafine nanoporous gold by low-temperature dealloying and kinetics of nanopore formation," *Appl. Phys. Lett.*, vol. 91, no. 8, pp. 2005–2008, 2007, doi: 10.1063/1.2773757.

[42] C. Alonso, R. C. Salvarezza, J. M. Vara, and A. J. Arvia, "The surface diffusion of gold atoms on gold electrodes in acid solution and its dependence on the presence of foreign adsorbates," *Electrochim. Acta*, vol. 35, no. 9, pp. 1331–1336, 1990, doi: 10.1016/0013-4686(90)85003-6.

[43] M. Hakamada, K. Tajima, K. Yoshimura, Y. Chino, and M. Mabuchi, "Solid/electrolyte interface phenomena during anodic polarization of Pd0.2M0.8 (M= Fe, Co, Ni) alloys in H2SO4," *J. Alloys Compd.*, vol. 494, no. 1–2, pp. 309–

314, 2010, doi: 10.1016/j.jallcom.2010.01.019.

[44] X. Wang, W. Wang, Z. Qi, C. Zhao, H. Ji, and Z. Zhang, “Fabrication, microstructure and electrocatalytic property of novel nanoporous palladium composites,” *J. Alloys Compd.*, vol. 508, no. 2, pp. 463–470, 2010, doi: 10.1016/j.jallcom.2010.08.094.